Two-dimensional simulations of a curved shock: Self-consistent formation of the electron foreshock

Philippe Savoini, Bertrand Lembège

JOURNAL OF GEOPHYSICAL RESEARCH, VOL. 106, NO. A7, PAGES 12,975–12,992, JULY 1, 2001

Two-dimensional simulations of a curved shock: Self-consistent formation of the electron foreshock

Philippe Savoini and Bertrand Lembège

Centre d'étude des Environnements Terrestre et Planétaires, CNRS,
Université de Versailles-St Quentin, Vélizy, France

Abstract. A collisionless curved shock is analyzed in a supercritical regime with the help of a two-dimensional electromagnetic full particle code. Curvature effects are included self-consistently and allow one to follow continuously the transition from a narrow and step-like strictly perpendicular shock to a wider and more turbulent oblique shock within the quasi-perpendicular range $65° < \theta_{Bn} < 90°$. Present results reproduce the formation of the electron foreshock without any simplifying assumptions. In agreement with experimental data, local bump-on-tail parallel distribution functions are well recovered in the foreshock region and correspond to electrons backstreaming along the magnetic field lines. Present detailed analysis shows that local back-streaming distributions have two components: (i) a high parallel energy component corresponding to back-streaming electrons characterized by a field-aligned bump-in-tail or beam signature, and (ii) a low-energy parallel component characterized by a loss cone signature (mirrored electron). Two types of bump-in-tail patterns, broad and narrow, are identified at short and large distances from the curved shock, respectively, and are due to different contributions of these two components according to the local impact of the time-of-flight effects. Present results allow one to identify more clearly the nature of the bump-in-tail pattern evidenced experimentally (narrow type). These also confirm that mirroring electrons make the dominant contribution to the bump-in-tail pattern in the total distribution in agreement with previous studies. Results suggest that low and high parallel energy populations are intimately related and may contribute together to the upstream wave turbulence.

1. Introduction

The foreshock is the region of space extending between the curved shock layer and the upstream magnetic field lines tangent to the shock; this region is characterized by the presence of energetic particles backstreaming upstream away from the shock front along magnetic field lines connected to the curved shock. Since the early seventies, this region has been extensively studied both theoritically [*Leroy and Mangeney*, 1984; *Wu*, 1984; *Cairns*, 1987; *Krauss-Varban and Wu*, 1989; *Fitzenreiter et al.*, 1990] and experimentally [*Filbert and Kellogg*, 1979; *Anderson et al.*, 1979; *Anderson*, 1981; *Parks et al.*, 1981; *Feldman et al.*, 1973, 1982, 1983; *Klimas*, 1985], and more recently, this region has been studied with the WIND spacecraft, which provides in situ measurements of high sensitivity and resolution [*Fitzenreiter et al.*, 1996; *Lepping et al.*, 1995; *Slavin et al.*, 1996; *Yin et al.*, 1998a], and the GEOTAIL mission [*Kasaba et al.*, 1997].

Paper number 2001JA900007.
0148-0227/01/2001JA900007$09.00

The general consensus is that the foreshock electron population is composed of incoming solar wind electrons and a small number of bow shock modified electrons that stream back into the upstream region. These backstreaming electrons have two components, which can be described in terms of time of flight and generalized mirroring processes as follows:

1. One component corresponds to electrons which, after interacting with the shock front, succeed to escape from the front and stream back along upstream magnetic field lines. Moreover, these electrons are convected back with magnetic field lines because of the earthward motion of the solar wind ($\vec{E} \times \vec{B}$ drift caused by the solar wind's motional electric field) and are spatially diffuse according to their parallel velocities. Then the velocity distribution at a given upstream observation point is the sum of contributions determined by velocity characteristics connecting different source points on the curved shock to the observer location. The effect analyzed by *Filbert and Kellog* [1979] and further developed by *Cairns* [1987] is called the time-of-flight mechanism.

2. The other component corresponds to electrons which are mirror reflected by the shock front. Indeed,

the shock front can be seen as a moving magnetic mirror structure, depending on which reference frame the process is viewed. It is convenient to discuss the mirror reflection process in the deHoffman-Teller (dHT) frame defined by a motional transformation along the shock surface in which the flow of the upstream plasma is parallel to the magnetic field and the induced motional electric field vanishes. Electron acceleration has been analyzed theoretically in dHT by *Leroy and Mangeney* [1984] and *Wu* [1984], who assumed an elastic encounter between electrons and a moving plane shock front. *Krauss-Varban and Wu* [1989] have shown that efficiency of this acceleration mechanism is similar in both dHT and normal incident (NI) frames. This energization mechanism is also called fast Fermi process [*Wu*, 1984] or gradient-B drift process [*Krauss-Varban and Wu*, 1989], since the reflection mechanism can be very efficient and does not require multiple interactions with the shock. The theory has shown satisfactory agreement with observational data and emphasizes the importance of the nearly perpendicular shocks as natural energizers of the solar wind electrons population.

In summary, theory predicts that electron energization by mirror effects is weakly sensitive to the shock structure but is quite sensitive to the shock wave geometry (through a $1/\cos\theta_{Bn}$ term), at least when the shock is nearly perpendicular; θ_{Bn} is the angle between the shock normal and the upstream magnetostatic field. Two main consequences can be deduced [*Leroy and Mangeney*, 1984; *Wu*, 1984]:

1. The average kinetic parallel energy per reflected electron increases rapidly with θ_{Bn} as:

$$< E_{r\parallel} > \approx 2m_e v^2_{\text{upstream}}/\cos^2\theta_{Bn} \qquad (1)$$

in the observer's frame.

2. In the case of an incoming Maxwellian distribution function, the density of reflected electrons decreases as $\exp[-1/\cos^2(\theta_{Bn})]$, when θ_{Bn} approaches 90°. As a consequence, the number of reflected electrons tends toward 0 at the leading edge of the foreshock, i.e., the magnetic field line tangent to the curved shock front. These calculations have been refined later by *Krauss-Varban and Wu* [1989], who expressed the gain of kinetic energy versus both the initial energy and pitch angle.

Even if a good qualitative agreement with observation is obtained, it is pertinent to resume the assumptions used in the analytical works which are not always justified:

1. The theory has been established for angles θ_{Bn} large enough to simplify the calculations and is only valid around 90°. Nevertheless, the acceleration mechanism is very sensitive to the angle θ_{Bn}, even a small deviation of θ induces strong variation of the energy gain (through the term $\cos^{-2}\theta_{\text{Bn}}$ of equation (1)).

2. Calculations ignore the effect of finite excursion time of electrons in the shock wave during reflection; in particular, no loss of energy due to waves-electrons interaction is considered during the reflection process.

3. The electron magnetic moment μ is assumed to be conserved in the reflection process (adiabatic theory). First, such an assumption is valid only when the gyroradius of a convected electron is much smaller than the width of the shock transition layer, which can be inaccurate for high inflow velocities. Second, the assumption does not account for magnetic and electric fluctuations seen by the particles during their time of flight in the vicinity of the shock front.

4. Shock front is assumed to be stationary. As already evidenced by planar one-dimensional (1-D) *Leroy et al.* [1982] for hybrid simulations and *Lembège and Dawson* [1987] for full-particle simulations and by two-dimensional (2-D) simulations [*Lembège and Savoini*, 1992], the shock front is nonstationary. Two sources of nonstationarity have to be considered [*Lembège and Savoini*, 1992]: First, the shock front suffers a self-reformation over a typical timescale of the order of the ion gyroperiod $< \tilde{\tau}_{ci} >_{\text{ramp}}$ (calculated from the mean value of the magnetic field in the ramp); second, the front itself exhibits a rippled pattern which moves in time along the shock front direction. Until now, the impact of this shock front nonstationarity on electron acceleration processes has not been analyzed and is still unknown.

More recently, analytical models of cylindrical and spherical shocks with zero and nonzero thickness have been investigated by *Vandas* [1995a, 1995b]. These studies examine the energy gain of reflected individual electrons in the presence of a curved shock in order to generalize theoretical results obtained in previous works. The model is based on strong assumptions. First, it solves electron motion in the shock layer with the adiabatic approximation, and it approximates the curved shock near the tangent point of the upstream magnetic field by a plane shock with varying B_n (the normal component of the magnetic field at the shock front). Second, it does not take into account the electrostatic field (E_{lx}) and the noncoplanar magnetic field in the shock layer, which are known to play an important role in the electron dynamic. In this model, the energy gain of reflected electrons is strongly affected by the curvature and, more particularly, is lower than that at a corresponding plane shock. Shock curvature decreases the time spent by the particle within the shock layer and so does its total energy gain. A comparison with experimental data leads to comparable levels of fluxes for interplanetary shocks but shows some discrepancies for the Earth's bow shock.

Numerical studies have already investigated the magnetic mirror reflection process with test particles and shock profiles issued from hybrid simulations [*Krauss-Varban and Wu*, 1989; *Krauss-Varban and Burgess*, 1991]. Simulations have been done with a one-dimensional hybrid code with macroparticle ions and an inertialess electron fluid to initiate a shock wave. Once

the shock is well established, energetic electrons which are assumed to participate in the reflection process are injected as test particles and are followed during several ion gyroperiods. Such simulations are not self-consistent, since this requires the use of full particle codes. In addition, these do not take into account the global curvature of a shock (which requires a 2-D geometry), and these only allow one to investigate the vicinity of 90° through a model where spatial curvature of the electromagnetic components is introduced via cosine functions. Both Maxwellian and κ functions are used to describe the incident electron population. A reasonable agreement is obtained with experimental data in producing the observed large fluxes of reflected electrons at the Earth's bow shock. Nevertheless, the intrinsic limitations of such hybrid simulations are obvious. The bow shock has a two-dimensional curved pattern, and electron foreshock cannot be reproduced with oblique planar shock simulations. In addition, reflected electrons back-streaming along the interplanetary magnetic field will experience a time-dependent angle θ_{Bn} which can modify the effectiveness of the acceleration process.

The purpose of the present paper is to present results obtained from full-particle simulations of a 2-D curved shock, where self-consistent features are fully involved and allow one to reproduce the electron foreshock without restrictive or ad-hoc assumptions.

The organization of the paper is as follows. Conditions of numerical simulations and the method for generating the curved shock are described in section 2. Section 3 presents the main numerical results; local electron distribution functions are analyzed in detail and are compared to experimental data in section 4. Finally, discussion and concluding remarks are given in section 5.

2. Numerical Description

Present simulations have been performed with a 2-1/2 dimensional, fully electromagnetic, relativistic particle code using standard finite-size particle techniques. Details have been already given by *Lembège and Savoini* [1992] and *Savoini and Lembège* [1994]. Basic properties of the numerical code can be summarized as follows. The simulation box is divided into two parts, vacuum and plasma. Fields are separated into two sets: The electromagnetic transverse components, hereinafter denoted by a subscript "*t*", reflect the induced effects and are solutions of the full set of Maxwells' equations, and the electrostatic longitudinal components, hereinafter denoted by a subscript "*l*", result from the space-charge effects and are solutions of Poisson's equation. Nonperiodic conditions are applied along the x direction within the simulation box and, periodic conditions are used along the y direction. Lengths of the plasma simulation box are $\widetilde{L}_x = 768$ and $\widetilde{L}_y = 1024$, which represent 40 and 53 ion inertial lengths ($\widetilde{c}/\widetilde{\omega}_{pi}$), respectively. All quantities with tildes are in normalized units.

The curved shock is created by using a cylindrical magnetic piston localized in the vacuum part of the simulation box. This procedure turns out to be very efficient and rapid in terms of computer time. The curved shock propagates through the $X-Y$ simulation plane as illustrated in Figure 1a.

One important point concerns the orientation of the magnetostatic field $\vec{B}_o$, which is partially lying outside the simulation plane. We define two angles as shown in Figure 1b: ϕ_o and θ_o provide the relative orientation of the magnetic field lines within and outside the $X-Y$ plane, respectively. More precisely, ϕ_o is defined between the projected $\vec{B}_o$ field (within the simulation plane) and X axis, while θ_o is defined between the magnetostatic field $\vec{B}_o$ and the projection of this field within the simulation plane.

The curvature of the shock front imposes a continuous variation in the orientation of the local shock normal $\vec{n}$ (always lying within the simulation plane, as illustrated by small arrows in Figure 1a); this implies an angle θ_{Bn} between the upstream magnetic field $\vec{B}_o$ and $\vec{n}$ defined by the relation:

$$\theta_{Bn} = \arccos\left[\cos\theta_o\left(\cos\phi_o\cos\phi + \sin\phi_o\sin\phi\right)\right], \quad (2)$$

where ϕ is the angle between $\vec{n}$ and the X axis. The present study is made for $\theta_o = 65°$ and $\phi_o = 45°$. The finite value of θ_o means that the curved shock is analyzed within a restricted quasi-perpendicular range, i.e., with θ_{Bn} varying from 90° to 65° where the electron acceleration is efficient, as ϕ varies from $\phi_o - 90°$ to ϕ_o.

Such a configuration provides the accessibility for the electrons to flow along the magnetic field lines outside the simulation plane and to have a moderate projected displacement within the $X-Y$ plane. Preliminary simulations have shown that the case $\theta_{Bn} = 0°$ (i.e., with $\vec{B}_o$ fully lying within the simulation plane, $\theta_o = 0°$) cannot be reproduced at present time with a reasonable CPU cost, since electrons flow immediately along the field lines before the curved shock is really formed.

The radius of the magnetic cylinder has been chosen carefully so that, after a short transient period $\widetilde{t} \leq 0.2\widetilde{\tau}_{ci}$, the curvature radius $\widetilde{R}_c$ of the shock is much larger than the ion Larmor radius, i.e., $\widetilde{R}_c \geq 34\widetilde{\rho}_{ci}$ ($\approx 200\widetilde{\rho}_{ce}$); $\widetilde{\tau}_{ci}$ is the upstream ion gyroperiod. Sizes of the simulation box and the time of the run are large enough to cover all characteristic space scales and timescales for both particle species ($\widetilde{t}_{\rm simul} = 1.1\widetilde{\tau}_{ci}$), and so that dynamics of the shock is independent of initial conditions. At the present stage of the study, it is important to point out that only the electron foreshock is investigated. The analysis of the ion foreshock is out of the scope of the paper, since it requires access to a larger angular region (below 65°) and also a much longer simulation time (several $\widetilde{\tau}_{ci}$).

The simulation follows 8,388,608 particles with a time step $0.06\widetilde{\omega}_{pe}^{-1}$ and an unrealistic mass ratio $m_i/m_e = 42$ (in order to save CPU time). Initial plasma condi-

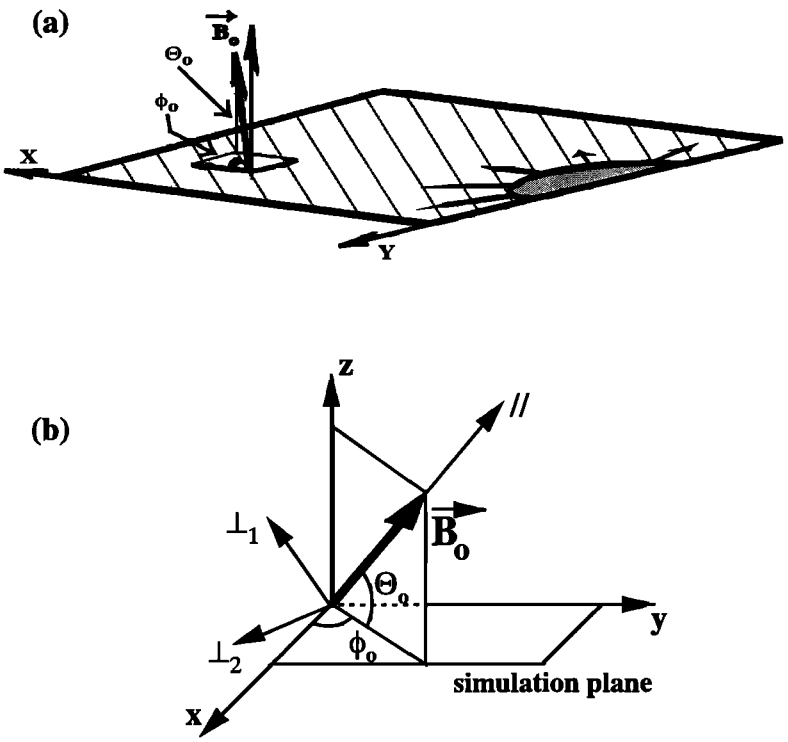

Figure 1. (a) Sketch of the reference set used in the 2-D simulation. Local $\vec{n}$ vectors normal to the curved shock front are illustrated by arrows. The magnetostatic field $\vec{B}_o$ is lying partially outside the simulation plane; its orientation is defined by two angles outside and inside the simulation plane, respectively namely, $\theta_o = 65°$ and $\phi_o = 45°$. For reference, straight lines represent the projection of the magnetic field lines within the simulation plan. (b) Details of the reference set used in the simulation code. In this study, directions $\|$, $\perp_1$, and $\perp_2$, are respectively defined with respect to the upstream magnetic field $\vec{B}_o$.

tions are summarized as follows: light velocity $\widetilde{c} = 3$, temperature ratio between ion and electron population $T_e/T_i = 1.58$, thermal momentum $\widetilde{p}_{\mathrm{the},\alpha} = 0.3$ for electrons (where α denotes the x, y, and z components, respectively) and $\widetilde{p}_{\mathrm{thi},\alpha} = 0.037$ for ions.

The ratio β of the kinetic to the magnetic pressure and the Alfvèn velocity are $\beta_e = 0.24$, $\beta_i = 0.15$, and $\widetilde{v}_A = 0.23$, respectively . The shock is in a supercritical regime; as reference, the Alfvèn Mach number measured at $\theta_{Bn} = 90°$ is $M_A = 3$.

3. Numerical Results

In order to clarify the presentation we will focus first on the salient features of the curved shock obtained in present 2-D simulations and, second, on the formation and characteristics of the electron foreshock

3.1. Salient Features of Curved Shock

Main characteristics of the self-consistent curved shock are illustrated in Figure 2, where are plotted time sequences of the profiles of the main magnetic component B_z versus distance through the shock front for different propagation angles, from $\theta_{Bn} = 65°$ to $\theta_{Bn} = 90°$. For reference, the $X - Y$ simulation plane is plotted (panel 0) at the last time of the run $\widetilde{t} = 1.1\widetilde{\tau}_{ci}$, on which are indicated the directions of the slices (straight lines) used for plotting the B_z profiles. The length of these slices in panel 0 corresponds to the length "d" of the sampling region used for the B_z profiles in the other panels.

In short, the well-known characteristics of a supercritical perpendicular shock, i.e., the foot-ramp-overshoot-undershoot pattern, are well recovered at $\theta_{Bn} = 90°$ (panel 5). A comparison with ion phase space (not shown here) confirms that the foot is well related to a noticeable number of reflected ions. An interesting feature is that the accumulation of reflected ions in time is responsible for the cyclic reformation of the shock front. This self-reformation has been already observed for a planar quasi-perpendicular shock in 1-D [*Lembège and Dawson*, 1987] and 2-D [*Lembège and Savoini*, 1992] full-particle simulations. The time period of this cyclic reformation is about $< \widetilde{\tau}_{ci} >_{\mathrm{ramp}}$. As emphasized by *Lembège and Savoini* [1992] with planar shock, this cyclic modulation (foot and overshoot) disappears for large deviations from 90°. Similar behavior is also evidenced for the present curved shock; no cyclic reformation persists for angles below $\theta_{Bn} = 85°$.

Several other features of a supercritical shock are well recovered in present simulations but are not detailed in the present paper. However, some quantitative results obtained herein stress the interest for simulating full

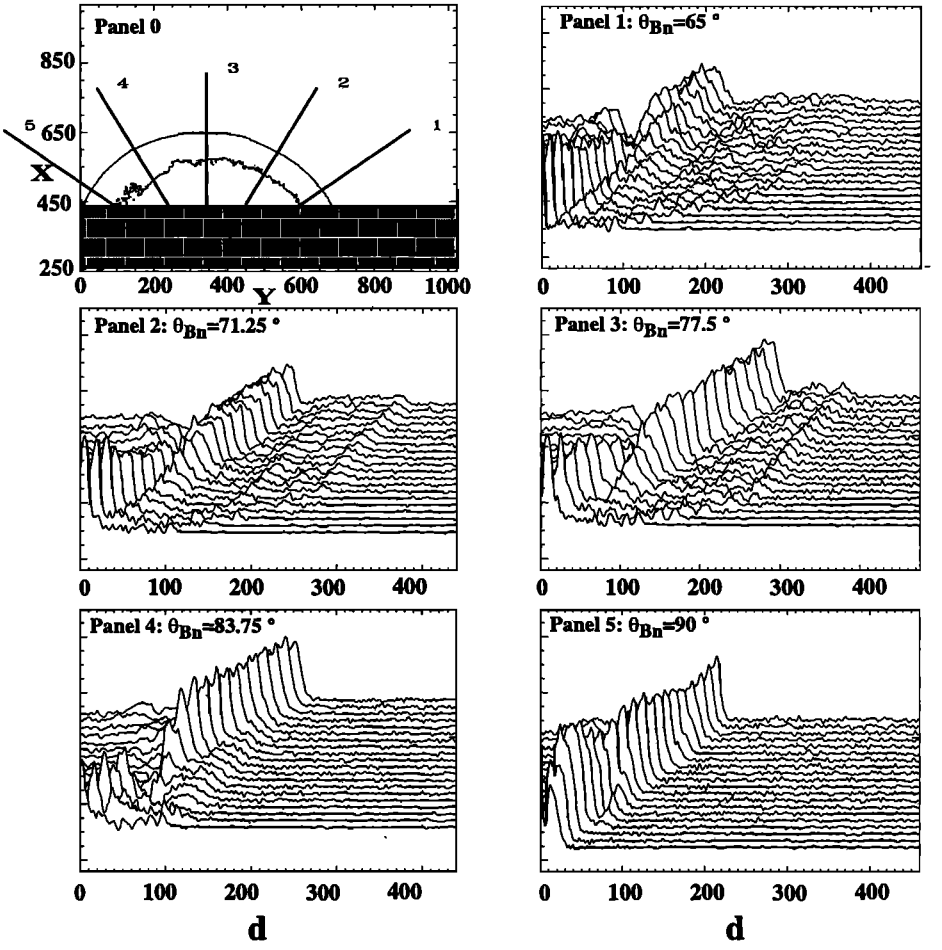

Figure 2. Time sequences of the local magnetic field component B_z versus distance d for different angles of propagation θ_{Bn} from 65° (panel 1) to 90° (panel 5). Within each panel the separation time between profiles is $\Delta\widetilde{t} = 24\widetilde{\omega}_{pe}^{-1}$. For reference, the location of the shock front within the $X - Y$ simulation plane is shown in panel 0 at a late time ($\widetilde{t} = 1.1\widetilde{\tau}_{ci}$); straight lines of length d (labeled 1-5) represent the different directions (slices) along which local profiles of B_z component are plotted in panels 1-5.

curvature effects of the shock in a self-consistent way. As expected, the magnetic field profile continuously evolves from a well-defined, step-like pattern (characterized by a narrow thickness) for $\theta_{Bn} = 90°$, to a more turbulent type profile (lying over a wider space range in the upstream region) as θ_{Bn} decreases. A turbulent field pattern appears upstream of the ramp for $\theta_{Bn} \leq 77.5°$. The identification and analysis of the upstream turbulence are out of the scope of this paper, but waves seem well correlated with the existence of the electron foreshock detailed in the section 3.2. Such an enhanced upstream turbulence is characteristic of a curved shock, since its level was much weaker in 1-D and 2-D planar simulations for similar plasma conditions even for a large deviation angle of the shock normal ($\theta_{Bn} = 55°$ from *Lembège and Savoini* [1992]). A further comparative analysis between planar and curved shocks will be required on this point.

Present study is restricted to the electron foreshock, which implies that other electron-ion foreshock mechanisms are not considered herein. The relative simplicity of the present foreshock formation related to one specie mainly (i.e., electrons) allows us to investigate in detail the basic physical processes involved into the generation and the acceleration of this particular population.

3.2. Main Features of the Electron Foreshock

For a comparison with numerical results it is useful to summarize briefly the characteristics of the electron foreshock as observed in the experimental data. Observations have confirmed many of the basic features of the electron foreshock which were observed or predicted earlier (*Filbert and Kellogg* [1979] for a first global picture; *Ogilvie et al.* [1971], *Feldman et al.* [1973]; *Anderson* [1981], *Fitzenreiter et al.* [1984, 1990, 1996]; *Yin et al.* [1998a], *Klimas* [1985], *Onsager and Thomsen* [1991] and *Fitzenreiter* [1995] for reviews and the references inside). Figure 3 [from *Fitzenreiter et al.*, 1990] is a good illustration of the local electron distribution func-

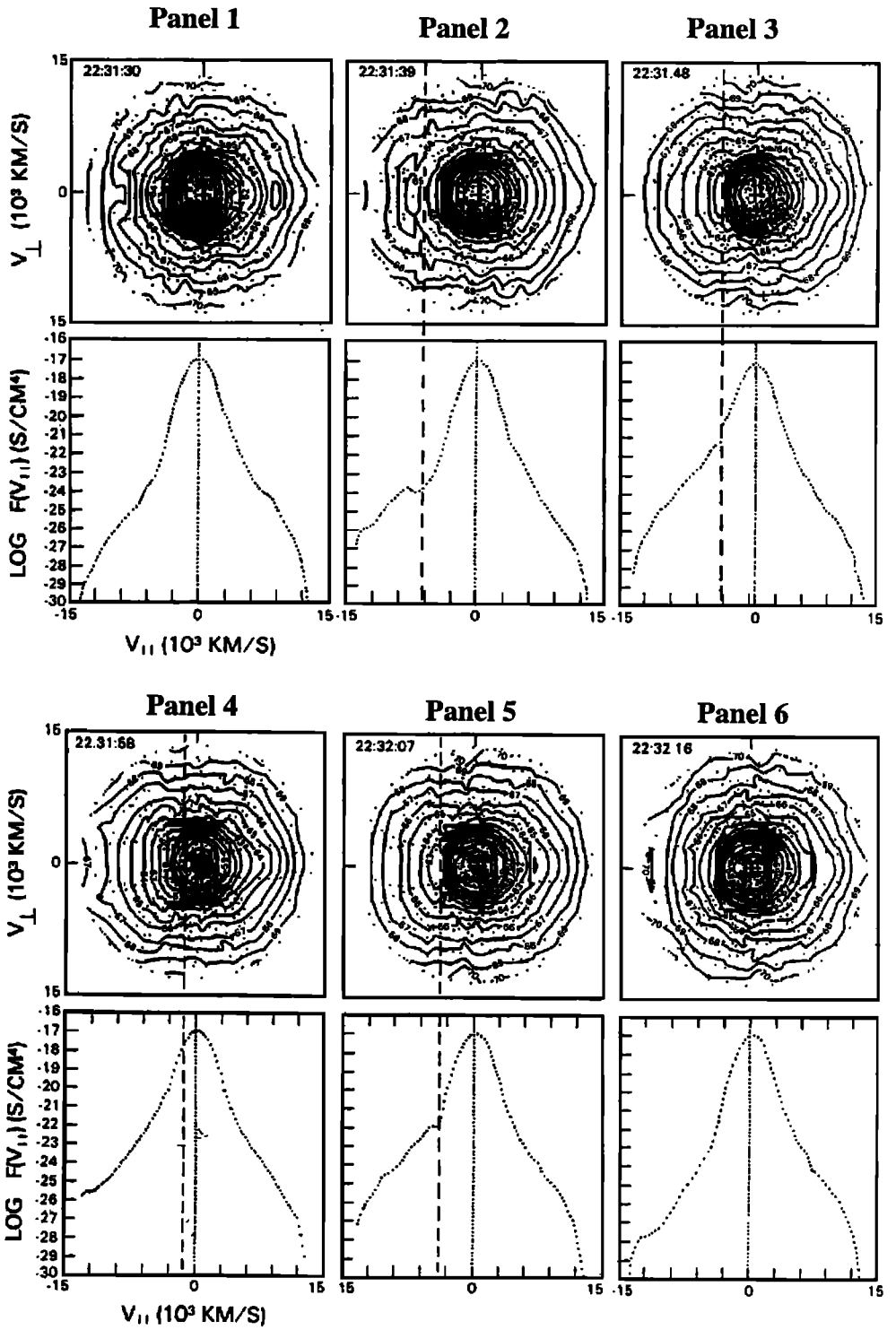

Figure 3. Local electron distribution measured by ISEE satellite when crossing the edge of the electron foreshock from [*Fitzenreiter et al.*, 1990]. Panels 1 and 6 correspond to measurements made in the solar wind, while panels 2-5 are for measurements at different distances within the foreshock. Panel 4 corresponds to a measurement made deeply within the foreshock.

tion measured by ISEE 1 from the solar wind (panels 1 and 6) into the electron foreshock (panels 2-5).

Near the leading edge of the foreshock, only electrons with high parallel velocities succeed to reach the upstream observation point. Other electrons with lower parallel velocity are swept downstream further from the leading edge by the incident solar wind flow. As a result, a secondary peak in the parallel electron distribution function is well observed when approaching the leading edge of the foreshock (panel 2). The resulting bump-on-tail distribution function is characteristic of the electron foreshock and was inferred as a source for

plasma wave emission associated with the electrostatic turbulence observed in the foreshock. In particular, beam-like streaming electrons have been shown to drive Langmuir-like waves near the local electron plasma frequency, which can be coupled to produce electromagnetic radiation near f_{pe} and $2f_{pe}$ [*Fredericks et al.*, 1971; *Scarf et al.*, 1971; *Canu*, 1989, 1990; *Bale et al.*, 1997; *Cairns and Robinson*, 1997; *Cairns et al.*, 1997; *Kasaba et al.*, 1997; *Schriver et al.*, 1997; *Yin et al.*, 1998b; *Cairns and Robinson*, 1999]. Deeper in the foreshock (less energetic), electrons escaping from the shock front do have less time to propagate far upstream, and the bump moves downward in parallel velocity until it disappears in the core of the distribution (panels 3 and 4). A deeper insight of Figure 3 suggests that two different populations may contribute to the local distribution function: a loss cone pattern (well evidenced at a certain distance from the leading edge) and a bump-in-tail pattern for high parallel energy electrons. All these characteristics of the Earth's electron foreshock have to be fully recovered in present 2-D self-consistent simulations.

The following procedure has been used for identifying the electron foreshock in our 2-D simulations, without any ad hoc assumption. One important step consists in determining as precisely as possible the energetic electron population backstreaming upstream away from the shock front. For so doing, three selection criteria have been used: (1) Electrons have to be upstream of the shock front at the end of the run; (2) these must have interacted with the shock front during the run time and (3) during this interaction, these are supposed to have gained enough energy to be differentiated from background ambient electrons. For the purpose of clarity these criteria may be presented in terms of two main successive conditions:

1. The first condition is the **selection in location**. First, at a late time of the run (herein, $1.1\widetilde{\tau}_{ci}$), one selects all electrons which are located upstream of the shock without any other a priori assumption. This electron population includes both all backstreaming electrons which have suffered reflection with the shock front at previous times and electrons located upstream to the shock front which did not yet interact with the shock front at that time. Second, among this population we select only those which are located in the area swept by the shock front during the simulation from an early time. This procedure eliminates all upstream electrons which did not yet interact with the shock front from this early time to late time $1.1\widetilde{\tau}_{ci}$.

2. The second condition is the **selection in energy**. One selects only those electrons which have gained enough kinetic energy in the acceleration processes to reach at least six times the initial thermal energy $\widetilde{E}_{\text{thermal}} = 0.135$.

The advantage of the present method is to eliminate safely electrons which do not have high contrast with respect to the background solar wind distribution, i.e., having a kinetic energy $\widetilde{E}_k < 0.8$. Some electrons contributing to the foreshock but having energy less than that imposed by the second criteria may be not selected. However, such a selection turns out to be safe enough to consider all selected electrons as the foreshock component, independently of their locations within the upstream region and/or of the energization processes responsible for their energetic backstreaming.

3.3. Identification of the Electron Foreshock Location

Figure 4a plots the locations of selected electrons at the end of the simulation ($\widetilde{t} = 1.1\widetilde{\tau}_{ci}$). As reference, the curved shock front is plotted in the X-Y simulation

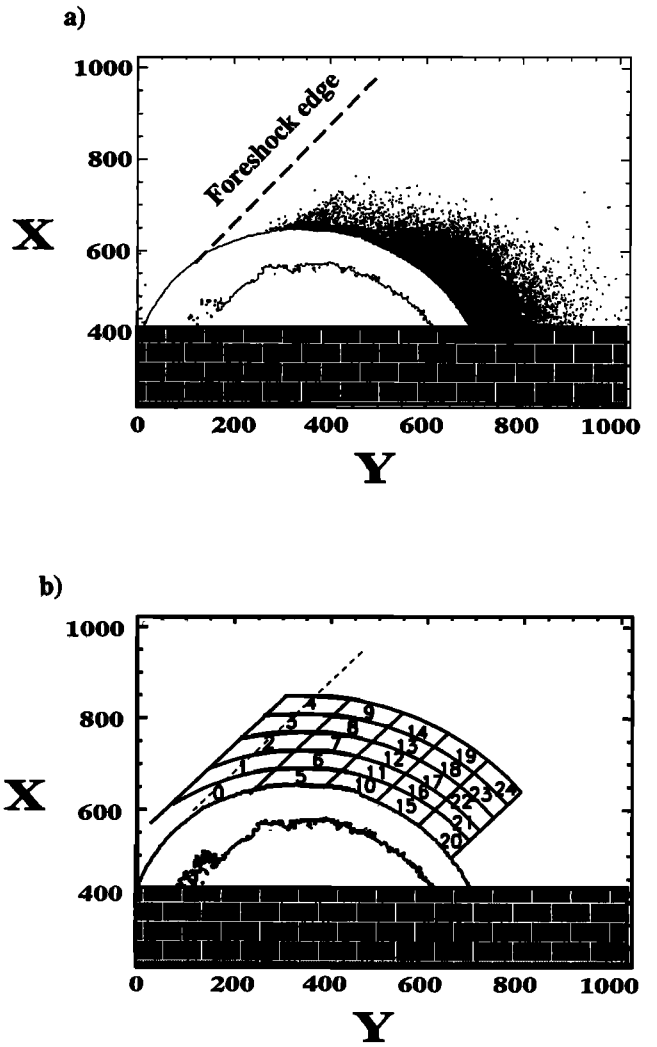

Figure 4. (a) Locations of foreshock electrons within the simulation plane at time $\widetilde{t} = 1.1\widetilde{\tau}_{ci}$. All these electrons are selected by both criteria used herein versus locations and kinetic energy, respectively (to see text), and the electrons are located upstream of the bow shock and within the edge of the foreshock. This foreshock limit fits quite well with the projected magnetic field line tangent to the curved front (thick dashed line). (b) Sketch showing the foreshock region sampled with 25 boxes (mainly aligned along the projected magnetic field lines) used to compute local electron distributions.

plane with the projected magnetic field line tangent to the bow shock, which defines the leading edge of the foreshock. Several important points may be stressed: First, all selected electrons are well located within the upstream region of the shock front and downstream to the tangent line. These characteristics fit quite well with the expected location of the electron foreshock. Second, these also confirm that high-energy electrons can be detected only within a restricted area upstream to the shock front. Third, as predicted by the theory, the density of selected electrons decreases drastically as θ_{Bn} increases to 90°. Only a few electrons are present when approaching the tangent line, in agreement both with theory [*Filbert and Kellogg*, 1979; *Cairns*, 1987; *Wu*, 1984; *Leroy and Mangeney*, 1984] and experimental observations [*Anderson et al.*, 1979; *Feldman et al.*, 1983; *Fitzenreiter et al.*, 1990]. The total number of backstreaming selected electrons represents $\approx$ 1% of the total number of the "incident" solar wind particles. However, let us note that this value does not represent strictly the real percentage of foreshock electrons, since some of these may be eliminated by the selection criteria used herein.

As evidenced in Figure 4a, no backstreaming electrons can be observed at the leading edge of the foreshock ($\approx$ 90°). This lack of particles can be due to either the physical reasons at the leading edge or the limited number of particles per cell used in the simulation. This particular region will be studied in more details by using a much higher number of particles per cell and/or by limiting the angle range of θ_{Bn} around 90° only, instead of 65° – 90°.

In order to analyze in detail the dynamics of backstreaming electrons, the overall foreshock area is divided into 25 small sampling boxes within which local electron distributions are computed. The extent of the whole upstream sampling region is restricted to limits where backstreaming electrons have been identified (Figure 4a is used as a reference). The size of each small sampling box has been chosen so that it is small enough to follow the progressive changes in local distributions (both in local angle θ_{Bn} and in distance with respect to the shock front) but large enough to satisfy some reasonable statistics. Shape and locations of sampling boxes are aligned along the magnetic field lines projected within the simulation plane as shown in Figure 4b. This disposal allows one to keep roughly the same size for all sampling boxes in order to reproduce a constant sampling rate performed in real satellite measurements. Then, five main different directions of sampling have been analyzed corresponding to boxes located nearest to the curved shock front (used as reference boxes); more precisely, these directions pass through the middle of the boxes. These correspond to directions $\theta_{Bn} \approx 90°$ (near the edge of the foreshock), 83.75°, 77.5°, 71.25°, and 65°, respectively, these are defined by boxes numbered 0, 5, 10, 15, and 20. Before presenting results on local distribution functions, it is important to check whether time-of-flight effects are correctly included in the present simulation frame.

3.4. Time of Flight Effects

Before comparing the numerical results with experimental data, it is worth pointing out that the time-of-flight effect described in the literature [*Asbridge et al.*, 1968; *Filbert and Kellogg*, 1979; *Cairns*, 1987; *Fitzenreiter et al.*, 1990] is fully included in the present simulation as illustrated in Figure 5.

The time-of-flight effect is an important feature of the foreshock and can be understood as a ballistic effect which is mainly due to the convection of the upstream magnetic field lines by the incoming solar wind which carries away the backstreaming electrons into the deeper region of the foreshock (Figure 5a). As a result, backstreaming electrons measured farther from the shock front come from different parts of the curved shock depending on their respective parallel velocity. Fast electrons come from the field line connected directly from the nearest point of the curved shock to

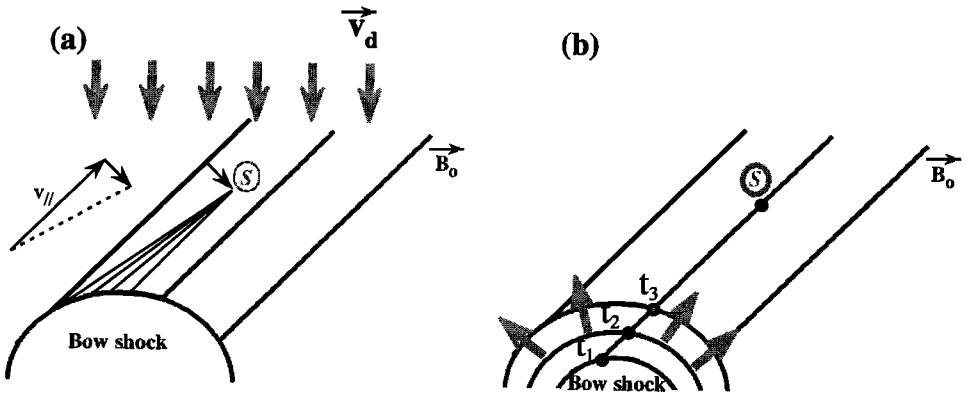

Figure 5. Sketch illustrating the comparison of time-of-flight effects in (a) observational results and (b) present numerical simulations. "S" indicates the location of an observer within the foreshock region. For reference, straight lines represent the projection of the magnetic field lines within the plane.

the observer location (S point), while slower electrons come from field lines connected from other parts of the curved shock to this S point. Then, the electron distribution function measured locally by a spacecraft in the upstream region includes electrons coming from different parts of the curved shock characterized by different θ_{Bn} propagation angles.

In the solar wind frame (i.e., frame of the present simulation) an equivalent situation is obtained as a given magnetic field line connected from the expanding curved shock to the observer point S will scan different angles θ_{Bn} in time, as illustrated by the shock normal directions at points t_1, t_2, and t_3 (see Figure 5b). Then, a direct comparison between experimental and numerical distributions can be performed and is reported in Figures 6, 8, 9, and 10.

4. Local Electron Distribution Function

Local distribution functions can be computed in the different sampling boxes by superimposing Figure 4b onto Figure 4a. It clearly appears that distribution functions cannot be measured accurately along the edge of the foreshock (boxes 1, 2, 3, 4, 8, and 9) and too far from the shock front (boxes 14-19), since the number of selected electrons is too low (or even null).

4.1. Total Distribution and Back-streaming Electron Distribution

Reduced parallel $f(p_{\|})$ distributions calculated from $f(p_{\|}, p_{\perp})$ are reported in Figure 6. Within each box, both the total distribution, hereinafter noted f_t (including solar wind and Back-streaming electrons), and the Back-streaming electrons' distribution, hereinafter noted f_b, are plotted. Let us note that the dotted line (representing the total distribution) is mixed with the solid line (representing the Back-streaming electrons) in the high-velocity range since it involves these energetic electrons. The comparison between Figures 3 and 6 shows a very good qualitative agreement with experimental data, which can be summarized as follows: The total parallel distribution $f_t(p_{\|})$ (dotted line) exhibits a characteristic bump-on-tail pattern observed *in-situ* in the different sampling boxes. For the purpose of clarity, we will analyze local distributions, first, versus progressive deviation from 90° and for boxes nearest to the curved shock front, and, second, versus relative distance from the shock front.

4.1.1. Variation versus angle. Sampling boxes versus angle near the shock front allow one to stress the following features:

1. In the vicinity of the leading edge (box 0), Back-streaming electrons have still low energy and are imbedded within the main core of the upstream undisturbed distribution; in addition, the number of these electrons is weak. These form a relatively cold (narrow) population animated with an averaged weak parallel drift velocity. No bump-in-tail pattern (or cold electron beam pattern) can be evidenced too near the leading edge of the foreshock.

However, for more oblique direction, the bump pattern is clearly identified and is even amplified quite well for large deviations from 90° (boxes 5, 10, 15 and 20). This is in contrast with the fact that it is expected to disappear more deeply within the foreshock. Such a discrepancy may be explained by remembering that more oblique direction (i.e., measurements made presently very near the curved shock front) should not be confused with measurements made more deeply within the foreshock as mentioned in experimental works. Such last measurements include also variation in distance with respect to the shock front itself, a fact which can be reproduced too by the present sampling measurements.

2. As angle deviates from 90°, the Back-streaming population has a much higher density, an increasing thermal momentum, and an increasing parallel drift momentum $< p_{\|} >$. These electrons mainly form a bump-in-tail with a momentum sign opposite to that observed in experimental data, since present simulations are in the solar wind frame. The relatively narrow extent of the field-aligned suprathermal distribution in box 0 becomes much broader (heating) as evidenced in boxes 5, 10, 15, and 20. This feature persists also at different distances from the shock front (boxes 6, 11, 16, and 21). Such a broadening evidenced with further penetration within the foreshock is in good agreement with the observations of *Feldman et al.* [1983].

3. Two different population components can be clearly identified in the Back-streaming population. When deviating from the leading edge of the foreshock, the well-pronounced, single-peaked distribution (P_1 in boxes 0 and 5) is progressively replaced by a double-peaked distribution (P_1 and P_2 in boxes 10, 15, and 20). This change has two consequences: First, this suggests the necessity for analyzing separately high and low parallel energetic electrons (as already mentioned for experimental results of Figure 3). This point will be developed in section 4.2. Second, with more oblique deviation, electrons of peak P_2 depart from the distribution tail and are responsible for the formation of a bump-in-tail around a finite-averaged parallel drift momentum. For large deviation from 90° this drift increases and reaches a maximum value $< p_{\|} > \approx 1.5$ (boxes 15 and 20); in contrast, peak P_1 stays always centered around a null drift velocity. When θ_{Bn} approaches 65°, the depletion between peaks P_1 and P_2 becomes partially filled in (box 20).

In summary, these results can be interpreted as a progressive transformation of the bulk energy of Back-streaming electrons into thermal energy as the direction with the shock normal is strongly oblique (boxes 5, 10, 15, and 20). Such features can be understood if one considers that electrons located around the leading edge of the foreshock (for instance, boxes 5 or 6) have been re-

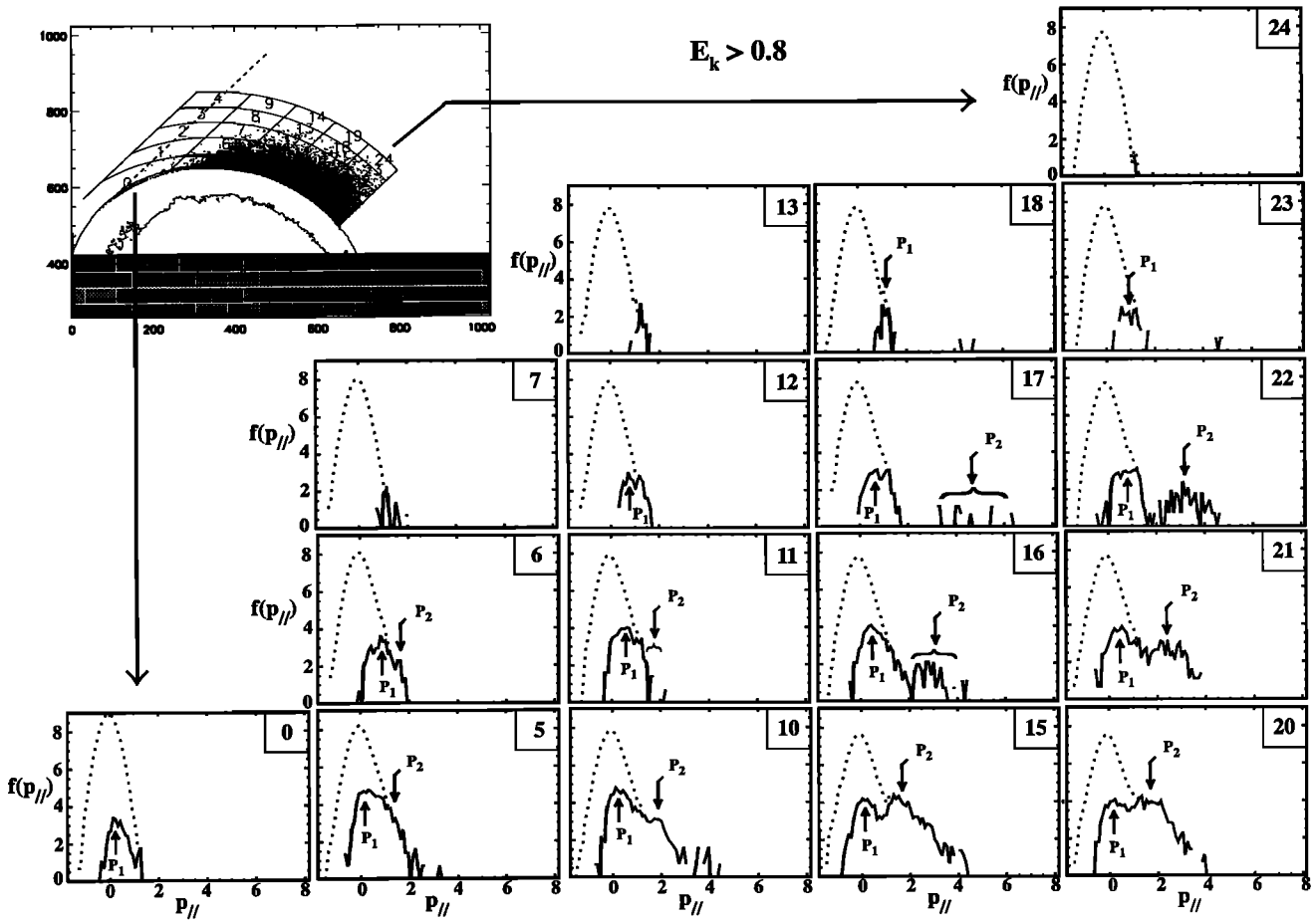

Figure 6. Local electron distribution functions $f(p_{\|})$ (in log scale) measured within the foreshock region sampled with 25 boxes, at time $\tilde{t} = 1.1\tilde{\tau}_{ci}$, where $p_{\|}$ is the parallel momentum. Total (dotted line) and backstreaming (solid line) electron distributions are represented respectively within each sampling box labeled from 0 to 24. For reference, the left-hand top panel shows locations of the curved shock front, of the backstreaming electrons, and of the sampling boxes within the simulation plane (see also Figure 4b for precise labels of sampling boxes); the foreshock edge is illustrated by the projected magnetic field line tangent to the curved front (dashed line)

flected (and accelerated) more recently than those of other groups. As a consequence, these did not have enough time to interact with the ambient solar wind plasma; this is in agreement with the absence of upstream turbulence observed as θ_{Bn} approaches 90° (see Figure 2). Then, results of boxes 0, 5, or 6 can be considered as characteristic distribution functions just after the reflection process and before driving various electrostatic and electromagnetic instabilities. In contrast, electrons of boxes located at more oblique angles have left the shock front much before those of boxes 0, 5, and 6 and have enough time to trigger some instabilities. As a consequence, these fluctuations cause some diffusion in energy (and in pitch angle) as shown in boxes 10, 15, and 20 and 11, 16, and 21. This behavior seems to be well confirmed by the presence of upstream electrostatic and electromagnetic wave activity evidenced for $\theta_{Bn} \leq 77.5°$ (Figure 2).

4.1.2. Variation versus distance. Let us consider the direction centered around the projected field line starting from the curved shock front at $\theta_{Bn} \approx 65°$. Results clearly show that the bump-in-tail (box 20) is progressively replaced by a well-pronounced beam pattern (separated from the main distribution) as the distance from the shock front increases (boxes 20-23). In other words, the parallel drift of high-energy electrons (peak P_2) strongly increases, that is, only the most energetic electrons can be observed at large distances from the shock front, but their density decreases rapidly with distance, and no field-aligned beam pattern can be identified too far from the front (box 24). As θ_{Bn} increases to 90°, the beam pattern can be partially identified over much shorter distances from the front, which can explain the difficulty for evidencing clearly such a local feature in experimental data. Similarly, low-energy electrons also suffer an increasing parallel drift (peak P_1) as the distance from both the foreshock edge and the bow shock increases. As a consequence, two different bump-in-tail patterns may be identified in the total distribution $f_t(p_{\|})$ at different locations where mecha-

nisms of formation largely differ; both patterns result from time-of-flight effects.

A relatively narrow bump-in-tail pattern is present both for large deviations from the leading edge of the foreshock and large angle; it is mainly due to the contribution of shifted peak P_1 (as in boxes 18 and 23). Such a distribution can also be observed for short deviation and nearer to the shock front (see boxes 6 and 11).

In contrast, for any oblique deviations from 90° but very near of the shock front, a much broadened bump-in-tail pattern is evidenced; it is only due to the contribution of the shifted peak P_2 (boxes 5, 10, 15, and 20). However, when penetrating deeply within the foreshock region (i.e., by combining both large deviations and large distance from the shock front), the resulting wide bump-in-tail pattern tends to be much narrower until being smoothed out within the total distribution for two combined reasons: absence of high-energy electrons (no P_2 peak) and finite parallel drift of low-energy electrons (i.e., peak P_1). These results illustrate the progressive disappearance of the bump-in-tail pattern to be compared with that evidenced in experimental data as detailed in section 5.

Unlike the parallel distribution, the perpendicular distribution $f_t(p_\perp)$ (not shown herein) exhibits a flat-top pattern which enlarges the tails of the incoming Maxwellian distribution. This feature is almost unchanged for any direction and almost any distance from the shock front. However, a loss cone type pattern appears at small oblique deviations from 90°; this will be analyzed in more details in section 4.2. At a large deviation from 90°, the only change in $f_t(p_\perp)$ is a slight decrease in the width of the flat-top distribution, as the distance from the curved shock front increases.

4.2. Low and High Parallel Energy Distributions

Until now, we have only analyzed the behavior of Back-streaming electrons according to their locations. Both experimental (Figure 3) and present numerical results (Figure 6a) emphasize differencies in the parallel distribution function which suggest that one perform a more detailed investigation of local distributions versus the level of parallel kinetic energy.

We have separated all selected Back-streaming electrons (Figure 4a) into two groups, with parallel kinetic energy $E_{k\|}$ higher and lower than 0.8. Locations of selected electrons are shown in Figures 7a and 7b, respectively. This selection in $E_{k\|}$ corresponds to momentum value $|p_\|| \approx 1.2$, where peak P_2 departs clearly from the tail of $f_t(p_\|)$ in box 10 of Figure 6. This procedure allows one to identify more clearly the characteristics of electrons contributing to peaks P_1 and P_2. It is important to stress that this selection does not invoke any assumption on the perpendicular velocity component. Again, one applies a spatial distribution of sampling boxes within the foreshock region (from boxes 1 to 24) identical to that used in Figures 4b and 6.

Figure 7 shows that results obtained in section 4.1 still persist for each separate population. First, density of each population strongly increases as θ_{Bn} decreases from 90° to 65°. Second, each population exhibits an effective limit near the foreshock edge along which density is almost null. However, important differences are evidenced between both populations and are summarized as follows:

4.2.1. Case $E_{k\|} \geq 0.8$ (Figures 7a and 8). High parallel kinetic energy electrons represent $\approx 26\%$ of f_b. The spatial distribution of these electrons is not homogeneous. These strongly accumulate along the projection of the magnetic field $\vec{B}_o$ in the simulation plane (Figure 7a), which corresponds to the extreme region of excursion where electrons can stream freely. These electrons are mainly responsible for the wide bump-in-tail in the total distribution $f_t(p_\|)$ at short distances of the shock front as shown in Figure 8. As discussed in section 4.1, this bump (peak P_2) is progressively replaced by a beam-like pattern in some regions of the foreshock. Corresponding perpendicular distribution

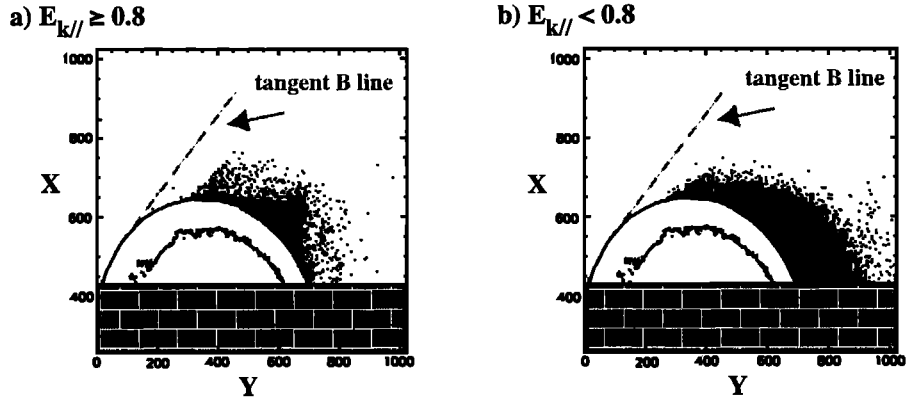

Figure 7. Locations of foreshock electrons within the simulation plane at time $\tilde{t} = 1.1\tilde{\tau}_{ci}$, for (a) high parallel kinetic energy and (b) low parallel kinetic energy. The foreshock edge is illustrated by the projected magnetic field line tangent to the curved front (dashed line).

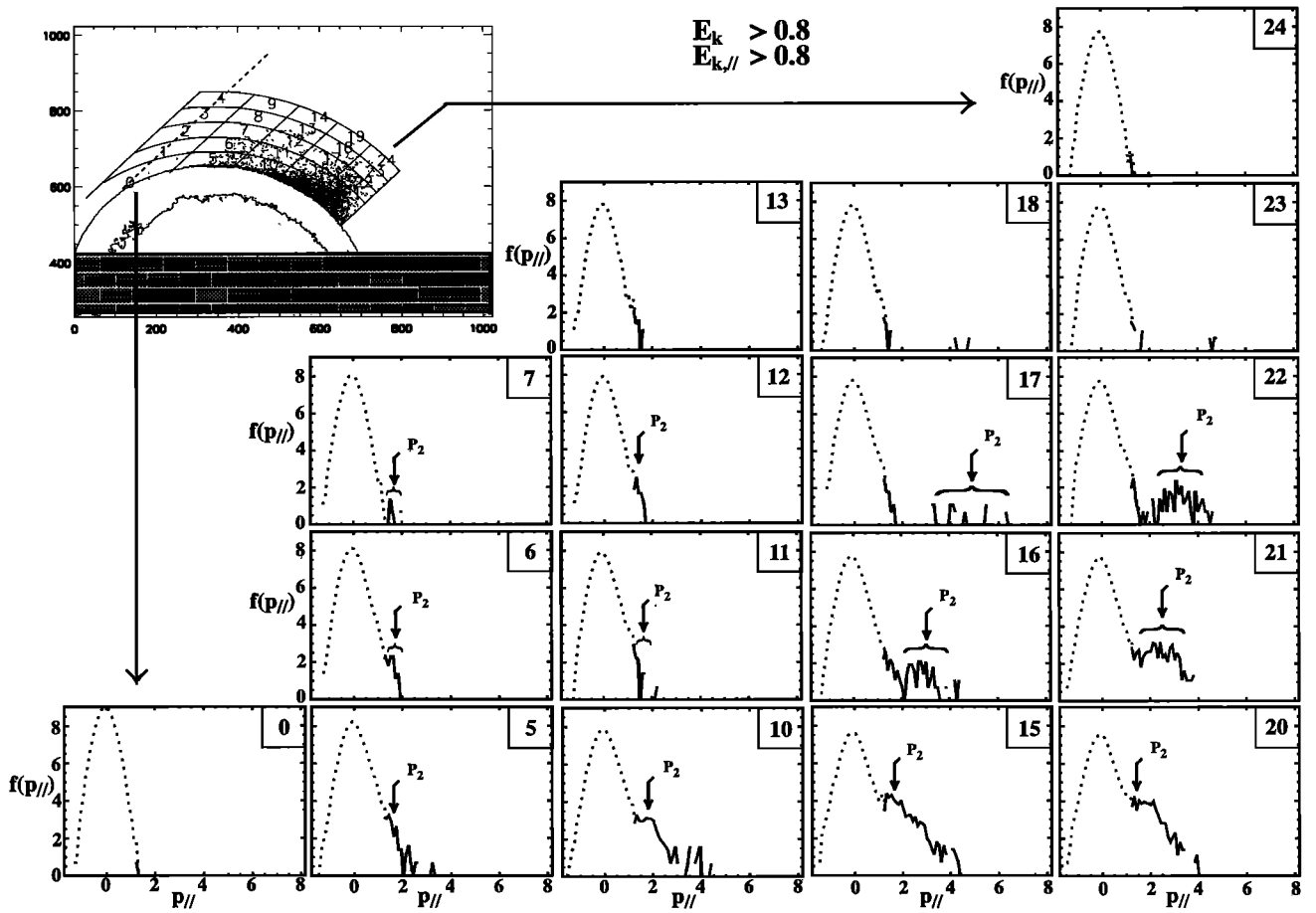

Figure 8. Figure similar to Figure 6 for backstreaming electrons selected with high parallel kinetic energy

$f^{\text{high}}(p_\perp)$ (not shown herein) does not exhibit any loss cone signature but rather a Gaussian-like shape (centered around 0). This shape tends to be replaced by a flat-top-like pattern as both propagation angle becomes more oblique and the distance increases from the shock front.

The absence of loss cone structure in the perpendicular distribution suggests different possibilities, which can be summarized as follow:

1. The reflection process for this population is not a mirror reflection, and another reflection mechanism has to be invoked to explain the observation of this high parallel energy electron component. One explanation is that electrons penetrate the shock front and find conditions for spending some time to interact with local macroscopic fields. Since the shock front is nonstationary and non-homogeneous, these may find some appropriate conditions to be reinjected upstream at later times and to escape with some energy high enough to be selected in the electron foreshock population.

2. The reflection process is a mirror reflection, and wave scattering destroys the loss cone signature until producing a Gaussian perpendicular distribution function. Absence of loss cone evidenced in our results almost everywhere could suggest a very efficient and rapid, local wave-particle scattering process. However, such a process has not enough time to produce a Gaussian shape as compared to the short time of electrons escaping from the front and propagating upstream along the magnetic field lines (formation of field-aligned beam or bump-in-tail even very close to the shock front). Nevertheless, the precise impact of the high wave activity observed upstream of the shock front on mirrored-reflected electrons has not been analyzed in details yet.

3. High-energy Back-streaming electrons correspond to leaked electrons (originating from the downstream region) which fill up the loss cone distribution (herein P_1 population). Indeed, electron leakage from the magnetosheath region has been invoked in previous works but seems not to be important [*Fitzenreiter et al.*, 1990]. One simplified approach to check this possibility is that after interacting locally with downstream waves, leaked electrons are supposed to have enough parallel energy to be able to overcome the electrostatic barrier in order to cross back the shock front from downstream to upstream region. By assuming that adiabatic invariant is conserved through the shock crossing, one expects that the perpendicular downstream temperature will be lower than its upstream value. For so doing, local distribution function has been calculated in sampling

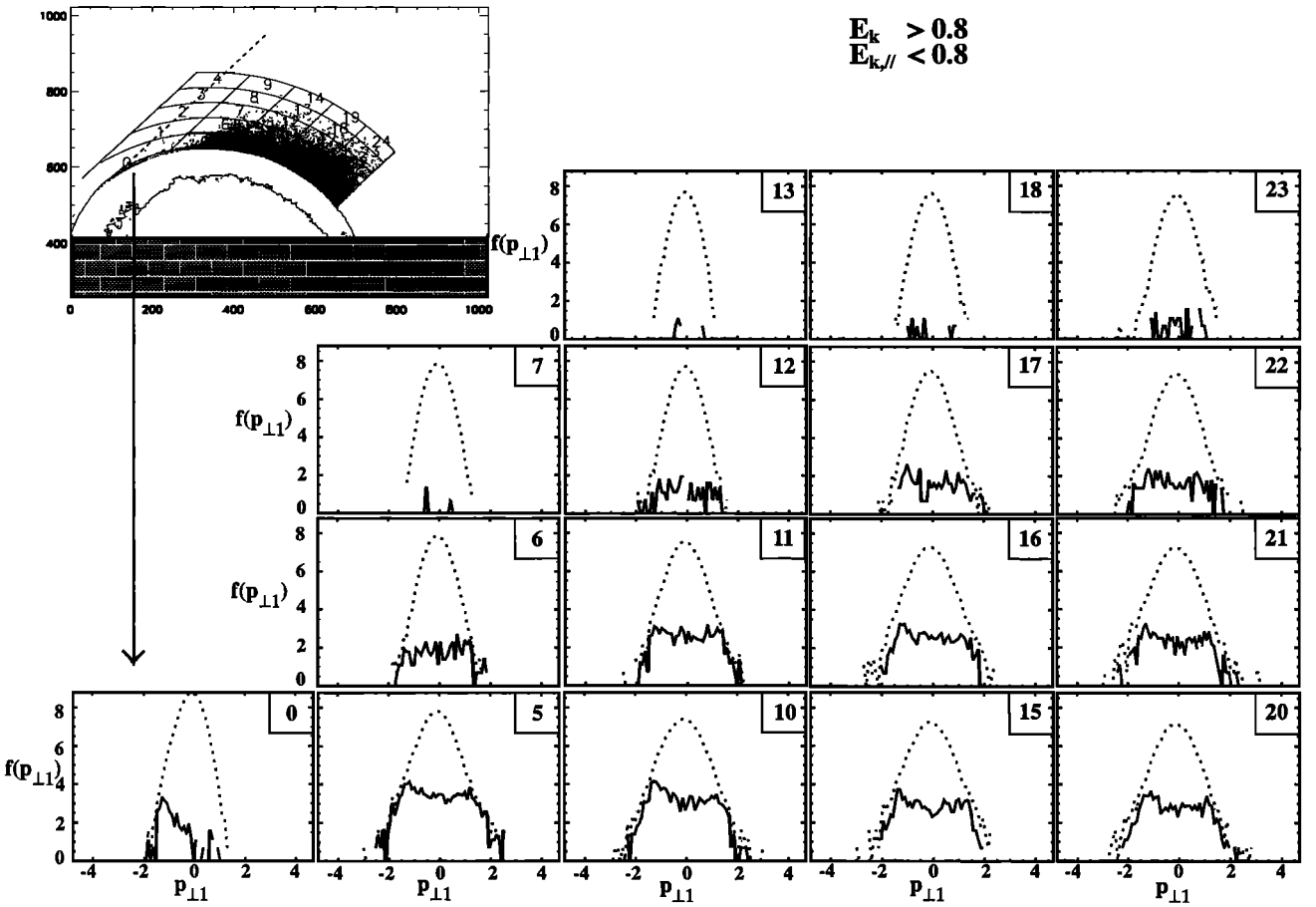

Figure 9a. Figure similar to Figure 6 for perpendicular distributions $f^{\text{low}}(p_{\perp 1})$ of backstreaming electrons selected with low parallel kinetic energy only, where $p_{\perp 1}$ is the perpendicular momentum component (direction defined in Figure 1b).

boxes extended from upstream (subscript "u") to downstream (subscript "d") regions. Both downstream and upstream perpendicular distributions exhibit Gaussian shape with associated temperature $T_{\perp d}$ (calculated for P_2 population only) and $T_{\|u}$, respectively. Results show that $T_{\perp d}/T_{\|u} = 0.9$, which contradicts conservation of the first adiabatic invariant (with a magnetic jump $B_d/B_u = 2.7$). Then, by default, present results do not support a leakage process from the magnetosheath as being dominant, since it does not account for the perpendicular distribution of the high-energy P_2 population; rather, this result supports that wave-particle scattering (upstream turbulence) may contribute to this population.

A more rigorous approach is necessary, and all three possibilities can be fully analyzed by following the time histories of reflected electrons; this work is left for a further study. At the present time, the respective contribution of the two main dominant processes invoked herein, namely, acceleration by macroscopic fields at the shock front and wave-particle scattering by upstream turbulence, is not yet determined.

4.2.2. Case $E_{k\|} < 0.8$ (Figures 7b and 9). The behavior of low parallel kinetic energy electrons is completely different, which means that different reflection mechanisms must be invoked. This population forms the main part of the f_b population ($\approx$ 74%). In contrast with the previous population (Figure 7a), the spatial distribution of these electrons is relatively much more homogeneous (Figure 7b) throughout the whole electron foreshock region (although their density still strongly increases, as θ_{Bn} decreases from 90° to 65°). Characteristics of the corresponding parallel distribution function $f^{\text{low}}(p_{\|})$ correspond to those of peak P_1 (Figure 6) discussed in section 4.1.

Complementary information is obtained in studying the perpendicular component of the distribution function $f^{\text{low}}(p_{\perp})$ represented in Figure 9a. The striking feature is the evidence of a characteristic loss cone signature. It is important to remember that no selection criteria has been used on the perpendicular velocity component; in other words, such a pattern is the consequence of a real process. This allows us to claim that magnetic reflection process is the main source of the energization for this population. As is well known and described by the theory, magnetic reflection is responsible for loss-cone signature by selecting the most energetic electrons in the perpendicular direction. This

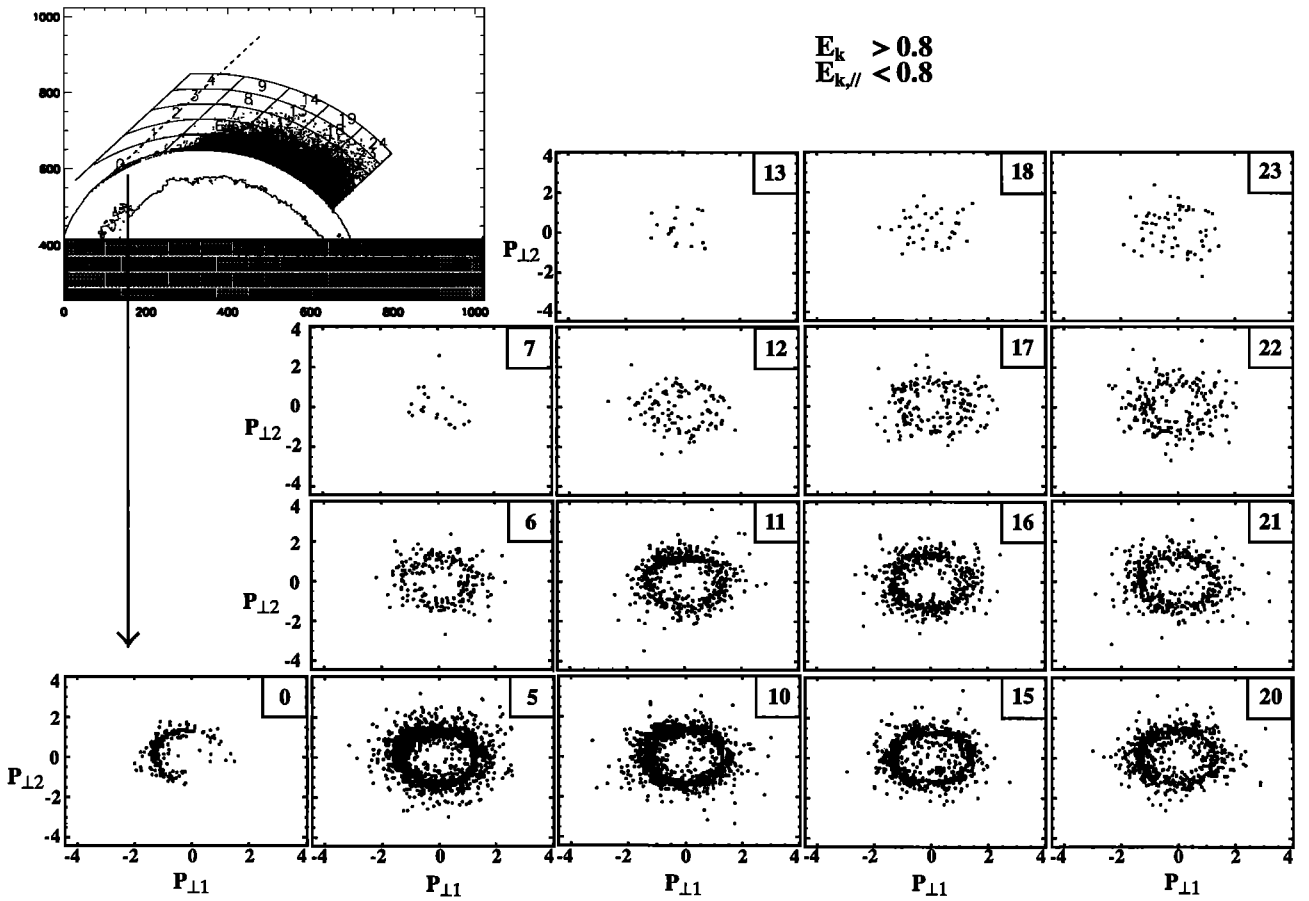

Figure 9b. Local ($\perp 1 - \perp 2$) electron momentum space corresponding to Figure 9a.

reflection process is expected to apply locally for all incident electrons, independently of the presence of the electromagnetic fields fluctuations. Present simulations confirm that a mirror reflection process produces local loss cone distribution at any point along the curved shock front (boxes 0, 5, 10, 15, and 20). Another important point is that loss cone patterns are also observed upstream at almost any distances within the foreshock region. Only the last far off boxes (boxes 13, 18, and 23) show nonevident loss cone distribution; indeed, the number of reflected electrons found in these boxes is too small to get a good statistic. Nevertheless, a more detailed picture can be obtained by analyzing the local perpendicular momentum space.

As expected, the loss cone signature is characterized by an electron ring well evidenced in the corresponding local sampling boxes of Figure 9b. More precisely, analysis of box 0 shows that the ring is not completely formed at that location, since it corresponds to the newly reflected electrons, and the resulting loss cone has an asymmetrical pattern (Figure 9a).

Evidence of the electron ring deeply in the foreshock region is in very good agreement with observations obtained by WIND experimental data [*Larson et al.*, 1996; *Lin et al.*, 1997]. This indicates that the mirror reflection process is quite efficient, since the loss cone pattern persists in time and space, even if some partial filling (also observed in the hole of the corresponding electron ring in Figure 9b) is evidenced. Electrons do not have enough time to interact noticeably with upstream fluctuations until smoothing out totally the loss cone pattern, even at locations where these fluctuations are the largest (boxes 10, 15, 20, 11, 16, and 21). Nevertheless, Figure 9b shows that at large distances within the foreshock (boxes 12, 18, and 23), electron ring is not clearly evidenced but becomes rather diffuse; this would indicate that diffusion processes may be more important, a fact which requires a deeper analysis since local statistics are too poor in the present case.

5. Discussion and Conclusions

To the knowledge of the authors, this work presents the first 2-D electromagnetic full-particle simulations of a curved shock, where self-consistent and kinetic effects of both particle species are fully involved; inhomogeneity effects and nonstationary behavior of the shock front are also involved self-consistently. Only one previous simulation work [*Thomas and Winske*, 1990] has reported results on self-consistent shock including curvature effects. This work was based on the use of a 2-D hybrid code which does not include electron dynamics

(introduced as massless fluid); the study was focused on the ion foreshock and on determining the locations of ion sources feeding the ion foreshock.

Some preliminary results of our 2-D full particle simulations of the curved shock have been presented in a previous paper [*Savoini and Lembège*, 1999]. The present study is focused on a detailed analysis of the electron foreshock, which is fully reproduced without any restrictive or a priori assumption. It is motivated by the fact that the curvature geometry and different spatial scales and timescales are expected to have a great impact on the particle acceleration mechanism; these have to be included in a self-consistent way in order to study the foreshock structure. The present key results are summarized as follows:

1. Features of electron foreshock generated by the interaction of upstream electrons with the shock are in good agreement with the picture provided by the compilation of a large amount of experimental data, except at the leading edge of the foreshock, where numerical limitations do not allow us to have a satisfactory statistic. Foreshock is characterized by a backstreaming fraction of shock-heated solar wind electrons which fill out the region between a leading edge defined by the magnetic field line tangent to the shock and the bow shock itself. The number of these backstreaming particles increases as θ_{Bn} deviates from 90°; no backstreaming electrons are identified at and very near the foreshock edge. The characteristic bump-in-tail pattern is fully recovered in the total parallel distribution; its persistence is a characteristic feature of the electron foreshock region, in good agreement with experimental observations [*Klimas and Fitzenreiter*, 1988; *Fitzenreiter et al.*, 1990; *Fitzenreiter*, 1995]. The density of backstreaming electrons decreases with increasing distance from the shock front. As a consequence, there is a limit upstream far from the front where no bump-in-tail can be evidenced and only solar wind electrons are present; however, even at such a large distance, upstream turbulence still persists in good agreement with experimental observations [*Fitzenreiter et al.*, 1990; *Greenstadt et al.*, 1995].

2. Present results clearly evidence that local backstreaming electron distribution f_t includes two components: (1) A low parallel energy component f^{low} corresponding to mirror-reflected electrons characterized by a loss cone perpendicular distribution pattern and a corresponding ring distribution in momentum space. One important feature is the persistence of the unstable electron ring (even if partially diffused) almost throughout the whole foreshock region; this indicates that the mirror reflection process turns out to be much more efficient than any diffusion process able to relax the ring or to fill in the loss cone totally. (2) A high parallel energy component f^{high} characterized by a bump-in-tail parallel distribution. Mirror reflection is not the mechanism source of these electrons, since no loss cone (or ring) signature is observed in a perpendicular distribution. This reinforces the idea that this component corresponds to electrons, which, after interacting with the macroscopic fields at the shock front, succeed to escape and backstream freely upstream along the magnetic field lines; wave scattering (turbulence at the shock front and in upstream region) may also contribute to this component. Nevertheless, results suggest that a leakage process from the magnetosheath is not a main candidate to account for the formation of this population. In addition, the present results confirm that a smoothed (stable) distribution is observed rather than an abrupt bump-in-tail or beam pattern, in agreement with the analysis of *Cairns* [1987], *Klimas and Fitzenreiter* [1988], and *Yin et al.* [1998a, 1998b]. This smoothed bump is also persistent almost throughout the whole foreshock region. This bump is only partially replaced by a field-aligned beam at large distances both from the shock front and from the foreshock edge, i.e., in restricted locations where most energetic electrons can still survive and backstream freely along the projected magnetic field lines.

3. One striking point is that the unstable ring, or loss cone (defined for f^{low}), and the stable bump-in-tail pattern (defined for f^{high}) persist simultaneously at the same locations in the foreshock regions. More precisely, the ring is only partially diffused in contrast with the smoothed bump, which corresponds to a relaxed-type parallel distribution (i.e., strong diffusion). In addition, when penetrating further into the foreshock, the loss cone population acquires a slight parallel drift (peak P_1), while the width of the perpendicular distribution for the high-energy population (peak P_2) is slightly increasing with shapes changing from a Gaussian to a flat-top pattern. This suggests that both low and high parallel energy populations may be intrinsically related (by some cross-field and/or field-aligned diffusion processes), as the distance within the foreshock increases, i.e., where time-of-flight effects play an important role. In addition, one can stress that both populations are observed even at locations where electrostatic and electromagnetic upstream wave turbulence is present too; both unstable beam and ring patterns persist at strongly oblique directions (around 65° in present case), where the turbulence level is the largest.

Moreover, spacecraft observations have stimulated significant interest in beam-plasma instabilities (quasi-linear and nonlinear stages), in order to account both for this upstream wave activity and for the smoothed bump-in-tail pattern in the total distribution (as a relaxed shape of a beam-plasma system). Such interactions have been recently studied in detail with more refined models including time-of-flight effects *see, e.g., Yin et al.*, 1998a, 1998b). However, such effects have been inserted into the reduced parallel distribution only, by adapting different shapes of the bump-in-tail pattern in the total distribution f_t. The present results suggest that a further improvement can be performed by inserting full 3-D, and not only parallel, momentum features in f_t distribution. Total f_t includes incom-

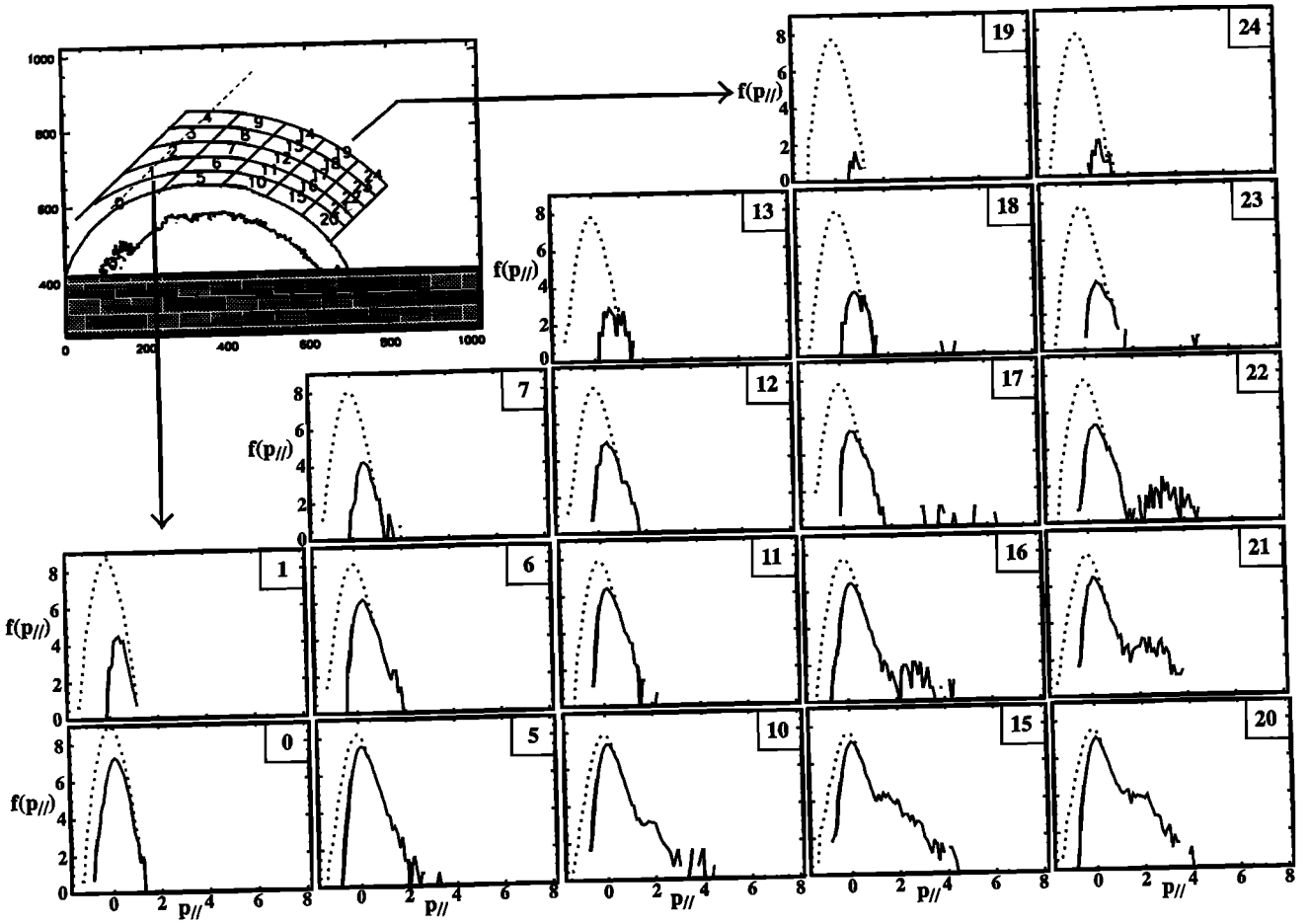

Figure 10. Figure similar to Figure 6 for foreshock electrons selected by the criteria on locations only (see text).

ing solar wind electron distribution and backstreaming electrons f_b distribution. Two components should be included for describing f_b distribution: (1) a low parallel energy component f^{low} with a broad bump-in-tail for $f^{low}(p_{\|})$ and an unstable ring distribution for $f^{low}(p_{\perp 1}, p_{\perp 2})$ and (ii) a high parallel energy component f^{high} with a narrow bump-in-tail for $f^{high}(p_{\|})$ and distribution $f^{high}(p_{\perp 1}, p_{\perp 2})$ varying from a Gaussian to a flat-top shape. The 3-D momenta features should be adjusted separately for f^{low} and f^{high} distributions in order to include appropriately the time-of-flight effects, similarly to that of *Yin et al.* [1998a, 1998b]. Such a complete description would allow one to include any cross-field/field-aligned diffusion processes and time-of-flight effects.

4. One confirms quite well that the bump-in-tail pattern in $f_t(p_{\|})$ tends to be smoothed out when penetrating further within the foreshock region, in good agreement with previous observations. However, the present study stresses that the comparison with experimental results requires a certain care. More precisely, two complementary points may be emphasized. On one hand, two different bump-in-tail patterns, broad and narrow, have been identified in the total parallel distribution at short and large distances from the bow shock, respectively. These patterns are due to the complementary contributions of the low and high parallel energy populations respectively, according to the local time-of-flight effects. On the other hand, the present results show that the narrow bump-in-tail pattern has different origins according to the distance both from the foreshock edge and from the bow shock itself at which the measurement is performed; it can be related to electrons of low or high parallel energy. Most of the bump-in-tail patterns have been observed experimentally at a certain distance from the shock front and correspond to the narrow type; in other words, mirroring electrons make the dominant contribution to the observed bump in $f_t(p_{\|})$ in a good agreement with conclusions of *Fitzenreiter et al.* [1990].

5. Moreover, one can wonder about the impact of the selection criteria used herein on the present results. For so doing, we have calculated the local distribution function without using the criteria on electron kinetic energy; only criteria on electron locations mentioned in section 3.2 have been applied. A consequence is that statistical sampling of local distributions is much better in Figure 10 and is more suitable to be compared with experimental results (where no selection criteria in energy range are used). However, one has to point out

that such a selection does not eliminate solar wind electrons which did not interact with the shock front during its expansion. Corresponding results confirm all the main results detailed in section 4; in particular, the total distribution has a narrow bump-in-tail which tends to be smoothed out with further penetration within the foreshock.

6. Obviously, there are a number of issues which require further investigation. First, let us remember that without time-of-flight effects, a slightly diffuse ring is a sign of partial relaxation. In the present case, where time-of-flight effects play an important role, one still ignores whether electrons which partially fill in the hole of the electron ring in $f^{\text{low}}(p_{\perp 1}, p_{\perp 2})$ distribution correspond to ring electrons which suffer a partial diffusion by waves-particles interaction, or to electrons of f^{high} distribution which succeed to escape the shock front. In the last case such electrons may have initial perpendicular velocity low enough (i.e., not to be selected by the mirror reflection criteria) to penetrate the shock front, and such electrons succeed in interacting with the shock during a transit time period before being reinjected into the upstream region with a parallel kinetic energy high enough but not too large in order to satisfy locally the energy criteria $E_{k\parallel} < 0.8$.

Second, the local escaping conditions for producing high parallel energy electrons have not yet been analyzed. Indeed, it is well known that shock curvature can strongly interfere with the production of energetic electrons. Electrons in the reflection process experience an average θ_{Bn} in the shock layer which greatly reduces the energy gain. Particle drift along the shock front has to be analyzed in the presence of spatial and/or temporal variations of the global shock front ("ripples") which are observed self-consistently in the simulation. The electrostatic potential at the shock front is expected to play an important role; moreover, the impact of this potential in the energy gain of mirror-reflected electrons (and in the enlargement of the loss cone angle) needs also to be analyzed in detail in order to be compared to theoretical approaches [*Leroy and Mangeney*, 1984; *Wu*, 1984; *Krauss-Varban and Wu*, 1989].

Third, only a part of the quasi-perpendicular domain has been investigated herein from 90° to 65°, and a larger angular range is necessary in order to investigate more oblique curvature effects (for example, from 90° to 45° in order to cover the full quasi-perpendicular range). Answers to the two first questions are possible by analyzing carefully the time trajectories of self-consistent backstreaming electrons; the answer to the third one is strongly dependent on updated supercomputer capacities. These different points are out of the scope of the present paper and are presently under active investigation.

Acknowledgments. Simulation runs have been performed on the CRAY *C*98 of the supercomputer center IDRIS located at Orsay. Thanks must be addressed to Jean-Noel Leboeuf for having provided the basic (periodic) version of the 2-D code. Thanks are also addressed to J. M. Teuler for his helpful computing assistance.

Michel Blanc thanks Richard Fitzenreiter and another referee for their assistance in evaluating this paper.

References

Anderson, K. A., Measurements of the bow shock particles far upstream from Earth, *J. Geophys. Res.*, 86, 4445–4454, 1981.

Anderson, K. A., R. P. Lin, F. Martel, C. S. Lin, G. K. Parks, and H. Reme, Thin sheets of energetic electrons upstream from the Earth's bow, shock. *Geophys. Res. Lett.*, *6*, 401, 1979.

Asbridge, J. R., S. J. Bame, and I. B. Strong, Outward flow of protons from the Earth's bow shock, *J. Geophys. Res.*, *73*, 5777–5782, 1968.

Bale, S. D., D. Burgess, P. J. Kellogg, K. Goetz, and S. J. Monson, On the amplitude of intense langmuir waves in the terrestrial electron foreshock, *J. Geophys. Res.*, *102*, 11,281–11,286, 1997.

Cairns, I. H., The electron distribution function upstream from the Earth's bow shock, *J. Geophys. Res.*, *92*, 2315–2327, 1987.

Cairns, I. H., and P. A. Robinson, First test of stochastic growth theory for langmuir waves in Earth's foreshock, *Geophys. Res. Lett.*, *24*, 369, 1997.

Cairns, I. H., and P. A. Robinson, Strong evidence for stochastic growth of langmuir-like waves in Earth's foreshock, *Phys. Rev. Lett.*, *82(15)*, 3066–3069, 1999.

Cairns, I. H., P. A. Robinson, R. R. Anderson, and R. J. Strangeway, Foreshock langmuir waves for unusually constant solar wind conditions: Data and implications for foreshock structure, *J. Geophys. Res.*, *102*, 24,249–24,264, 1997.

Canu, P., Linear study of the beam-plasma interaction as a source mechanism for the broadband electrostatic emissions observed in the electron foreshock, *J. Geophys. Res.*, *94*, 8793–8804, 1989.

Canu, P., Oblique broadband electron plasma waves above the plasma frequency in the electron foreshock: Linear theory and spacecraft observations, *J. Geophys. Res.*, *95*, 11,983–11,991, 1990.

Feldman, W. C., J. R. Asbridge, S. J. Bame, and M. D. Montgomery, Solar wind heat transport in the vicinity of the Earth's bow shock, *J. Geophys. Res.*, *78*, 3697-3713, 1973.

Feldman, W. C., R. C. Anderson, J. R. Asbridge, S. J. Bame, J. T. Gosling, and R. D. Zwickl, Plasma electron signature of magnetic reconnection to the Earth's bow shock: ISEE-3, *J. Geophys. Res.*, *87*, 632–642, 1982.

Feldman, W. C., R. C. Anderson, S. J. Bame, S. P. Gary, J. T. Gosling, D. J. McComas, and M. F. Thomsen, Electron velocity distributions near the Earth's bow shock, *J. Geophys. Res.*, *88*, 96–110, 1983.

Filbert, P. C., and P. J. Kellogg, Electrostatic noise at the plasma frequency beyond the Earth's bow shock, *J. Geophys. Res.*, *84*, 1369–1381, 1979.

Fitzenreiter, R. J., The electron foreshock, *Adv. Space Res.*, *15(8/9*, 9–27, 1995.

Fitzenreiter, R. J., A. J. Klimas, and J. D. Scudder, Detection of bump-on-tail reduced electron velocity distributions at the electron foreshock boundary, *Geophys. Res. Lett.*, *11*, 496–499, 1984.

Fitzenreiter, R. J., J. D. Scudder, and A. J. Klimas, Three-dimensional analytical model for the spatial variation of the foreshock electron distribution function: Systematics

and comparisons with ISEE observations, *J. Geophys. Res.*, *95*, 4155–4173, 1990.

Fitzenreiter, R. J., A. F. Vinas, A. J. Klimas, R. P. Lepping, M. L. Kaiser, and T. G. Onsager, WIND observations of the electron foreshock, *Geophys. Res. Lett.*, *23*, 1235–1238, 1996.

Fredericks, R. W., F. L. Scarf, and L. A. Frank, Nonthermal electrons and high-frequency waves in the upstream solar wind, 2, Analysis and interpretation, *J. Geophys. Res.*, *76*, 6691–6699, 1971.

Greenstadt, E. W., G. K. Crawford, R. J. Strangeway, S. L. Moses, and F. V. Coroniti, Spatial distribution of electron plasma oscillations in the Earth's foreshock at ISEE-3, *J. Geophys. Res.*, *100*, 19,933–19,940, 1995.

Kasaba, Y., H. Matsumoto, Y. Omura, and R. R. Anderson, Geotail observation of $2f_{pe}$ emission around the terrestrial electron foreshock, *Adv. Space Res.*, *20*, 699, 1997.

Klimas, A. J., The electron foreshock, in *Collisionless shocks in Heliosphere: Reviews of Current Research, Geophys. Monog. Ser.*, vol 35, edited by B. T. Tsurutani R. G. Stone, pp 237–252, AGU, Washington, D.C., 1985.

Klimas, A. J., and R. J. Fitzenreiter, On the persistence of unstable bump-on-tail electron velocity distributions in the Earth's foreshock, *J. Geophys. Res.*, *93*, 9628–9648, 1988.

Krauss-Varban, D., and D. Burgess, Electron acceleration at nearly perpendicular collisionless shocks, 2. Reflection at curved shocks, *J. Geophys. Res.*, *96*, 143–154, 1991.

Krauss-Varban, D., and C. S. Wu, Fast fermi and gradient drift acceleration of electrons at nearly perpendicular collisionless shocks, *J. Geophys. Res.*, *94*, 15,367–15,372, 1989.

Larson, D. E., et al., Probing the Earth's bow shock with upstream electrons, *Geophys. Res. Lett.*, *23*, 2203–2206, 1996.

Lembège, B., and J. M. Dawson, Self-consistent study of a perpendicular collisionless and nonresistive shock, *Phys. Fluids*, *30*, 1767–1788, 1987.

Lembège, B., and Ph. Savoini, Non-stationarity of a 2-D quasi-perpendicular supercritical collisionless shock by self-reformation, *Phys. Fluids*, *B4(11)*, 3533–3548, 1992.

Lepping, R. P., et al., The wind magnetic field investigation, *Space Sci. Rev.*, *71*, 207, 1995.

Leroy, M. M., and A. Mangeney, A theory of energization of solar wind electrons by the Earth's bow shock, *Ann. Geophys.*, *2*, 449–456, 1984.

Leroy, M. M., D. Winske, C. C. Goodrich, C. S. Wu, and K. Papadopoulos, The structure of perpendicular bow shocks, *J. Geophys. Res.*, *87*, 5081–5094, 1982.

Lin, R. P., et al., Observations of the solar wind, the bow shock, and upstream particles with the wind 3D plasma instrument, *Adv. Space Res.*, *20(4/5)*, 645–654, 1997.

Ogilvie, K. W., J. D. Scudder, and M. Sugiura, Electron energy flux in the solar wind, *J. Geophys. Res.*, *76*, 8165–8173, 1971.

Onsager, T. G., and M. F. Thomsen, The Earth's foreshock, bow shock, and magnetosheath, *IUGG Gen. Assem., 20th, Vienna, Aust., Aug. 11-24*, *29*, 998–1007, 1991.

Parks, G. K., et al., Upstream particle spatial gradients and plasma waves, *J. Geophys. Res.*, *86*, 4343–4354, 1981.

Savoini, P., and B. Lembège., Electron dynamics in two and one dimensional oblique supercritical collisionless magnetosonic shocks. *J. Geophys. Res.*, 99, 6609–6635, 1994.

Savoini, P., and B. Lembège. Full curvature effects of a collisionless shock, *Adv. Space Res.*, *24(1)*, 13–22, 1999.

Scarf, F. L., R. W. Fredericks, L. A. Frank, and M. Neugebauer, Nonthermal electrons and high-frequency waves in the upstream solar wind, 1, Observations, *J. Geophys. Res.*, *76*, 5126–5171, 1971.

Schriver, D., V. Sotnikov, M. Ashour-Abdalla, and V. Fiala, Two-dimensional saturation of broadband electron acoustic waves in the foreshock region, *J. Geophys. Res.*, *102*, 17,451–17,457, 1997.

Slavin, J. A., A. Szabo, M. Predo, R. P. Lepping, R. J. Fitzenreiter, K. W. Ogilvie, C. J. Owen, and J. T. Steinberg, Near-simultaneous bow shock crossings by WIND and IMP 8 on December 1, 1984, *Geophys. Res. Lett.*, *23*, 1235–1238, 1996.

Thomas, V. A., and D. Winske, Two dimensional hybrid simulation of a curved bow shock, *Geophys. Res. Lett.*, *17*, 1247–1250, 1990.

Vandas, M., Acceleration of electrons by a nearly perpendicular curved shock wave, 1, Zero shock thickness, *J. Geophys. Res.*, *100*, 21,613–21,621, 1995a.

Vandas, M., Acceleration of electrons by a nearly perpendicular curved shock wave, 2, Nonzero shock thickness, *J. Geophys. Res.*, *100*, 23,499–23,506, 1995b.

Wu, C. S., A fast fermi process: Energetic electrons accelerated by a nearly perpendicular bow shock, *J. Geophys. Res.*, *89*, 8857–8862, 1984.

Yin, L., M. Ashour-Abdalla, J. M. Bosqued, M. El-Alaoui, and J. L. Bougeret, Plasma waves in the earth's electron foreshock: 1, Time-of-flight electron distributions in a generalized lorentzian plasma and dispersion solutions, *J. Geophys. Res.*, *103*, 29,595–29,617, 1998a.

Yin, L., M. Ashour-Abdalla, J. M. Bosqued, M. El-Alaoui, and J. L. Bougeret, Plasma waves in the earth's electron foreshock: 2, Simulations using time-of-flight electron distributions in a generalized lorentzian plasma, *J. Geophys. Res.*, *103*, 29,619–29,632, 1998b.

B. Lembège and P. Savoini, CETP/UVSQ, 10 - 12, Avenue de l'Europe, 78140 Vélizy, France. (Bertrand.LEMBÈGE@cetp.ipsl.fr; Philippe.SAVOINI@cetp.ipsl.fr)

(Received April 21, 2000; revised December 19, 2000; accepted December 20, 2000.)